

General Relativistic Hydrodynamic Simulations around Accreting Black Holes

Sudip K Garain^[0000-0001-9220-0744] and
Pranayjit Dey

Abstract Strong gravity in the immediate vicinity of compact objects (e.g., black holes, neutron stars) necessitates inclusion of general relativistic effects. Traditionally, pseudo-Newtonian potential representations of gravity were favored to simulate the fluid motion in this region since that reduced the calculation complexity. However, with the advent of easily implementable, reliable numerical algorithms and computer hardware, more and more research groups are shifting towards the numerical solutions of general relativistic fluid dynamics equations. In this work, we report our progress on the development of such simulation tool and present results of sub-Keplerian accretion flow onto black holes.

1 Introduction

Fluid configuration around the black holes determines the spectro-temporal and polarimetric signatures for stellar mass black hole X-ray binaries (BHXRBS) as well as the active galactic nuclei (AGNs) [1, 2]. Strong gravity around the black holes mostly dictates the fluid behaviour. Therefore, solution of general relativistic fluid dynamics equations are frequently used to infer the spectro-temporal as well as polarimetric properties.

Majority of the general relativistic simulations of accretion disk start from an initially equilibrium torus threaded with a seed magnetic field ([3] and references therein). However a more realistic simulation set up may be constructed by letting

Sudip K Garain

Department of Physical Sciences and Center of Excellence in Space Sciences India, Indian Institute of Science Education and Research Kolkata, Mohanpur, Nadia 741246, India , e-mail: sgarain@iiserkol.ac.in

Pranayjit Dey

Department of Physical Sciences, Indian Institute of Science Education and Research Kolkata, Mohanpur, Nadia 741246, India

the matter ideally come from far out and enter the simulation domain situated at a finite distance. Model based analytical solution for velocity components, pressure, density etc. can be supplied as the inflow boundary condition at the outer boundary of the simulation domain and the time-dependent fluid dynamical equations, with the help of this boundary condition, should determine the dynamical solution inside the domain. Accretion simulations of collapsing plasma with initially Bondi type spherically symmetric matter distribution, but with latitude-dependent low angular momentum (sub-Keplerian), has been done earlier using non-GR codes ([4, 5, 6]) and recently using GRMHD simulations ([7, 8, 9, 10]). We are, rather, interested in accretion simulations of axisymmetric, thick disk type configuration. Such set-up has been used to simulate sub-Keplerian and Keplerian matter accretion onto black holes [11, 12, 13, 14, 15, 16]. However, all these simulations are done using pseudo-Newtonian potential proposed by [17].

Our aim is to extend such simulations using general relativistic fluid dynamics solvers. A few general relativistic hydrodynamics (GRHD) simulations of transonic, sub-Keplerian accretion disk with this type of set-up have been conducted earlier [18, 19]. However, further extensions are not reported. We are in process of developing a three dimensional GRHD code, designed specifically to implement the above set-up, and in this paper, report the initial results using that code.

Our paper is organized as follows: In Section 2, we provide a very brief overview of the general relativistic analytical solution of sub-Keplerian accretion flow. In Section 3, we introduce the GRHD equations and our numerical solution methodology. In Section 4, we present the results. Finally, in Section 5, we provide concluding remarks.

In our following calculations, we use $r_g = GM_{bh}/c^2$ as unit of distance, r_g/c as unit of time and $r_g c$ as unit of specific (i.e., per unit mass) angular momentum. Specific energy is measured in the unit of c^2 . Here, G is the gravitational constant, M_{bh} is the mass of the black hole and c is the speed of light in vacuum.

2 Sub-Keplerian flow : Analytical solutions

The general relativistic analytical solutions for transonic, sub-Keplerian accretion flow onto compact objects are discussed in [20, 21, 22] with sufficient details. A non-dissipative, transonic accretion flow is usually characterized by the conserved parameters specific energy ($\epsilon = u_t/(1 - na_s^2)$) and specific angular momentum ($l = -u_\phi/u_t$). Here, u_t and u_ϕ are the t and ϕ components of the four-velocity u_μ , n is the polytropic index and a_s is the local sound speed.

The analytical solution aims to find the radial variation of the fluid variables under the stationary and axisymmetric conditions. The calculation starts by considering the equations of the conserved specific energy $\epsilon = u_t/(1 - na_s^2)$ and the mass accretion rate $\dot{m} = Au^r \rho$. Here, A is a geometric quantity representing the surface area through which mass flux is considered, u^r is the r component of the four-velocity u^ν and ρ is the rest mass density. Further, using the adiabatic equation of state $P = K\rho^\Gamma$,

with P being pressure and Γ being the adiabatic index, and the relation between enthalpy h and a_s as $h = 1/(1 - na_s^2)$, ϵ and \dot{m} are expressed in terms of a_s and the radial velocity \mathcal{V} in the rotating frame. Using the fact that ϵ and \dot{m} are conserved, by differentiating these equations w.r.t. r and eliminating da_s/dr , once can obtain an equation for $d\mathcal{V}/dr$ [18, 19]. Numerical integration of this equation will result in $\mathcal{V}(r)$ and subsequently all other fluid variables as a function of r .

3 General Relativistic Hydrodynamics: Basic equations and solution procedure

For numerical simulations, we solve the following conservation equations:

$$\nabla_\mu (\rho u^\mu) = 0 \quad (1)$$

$$\nabla_\mu T^{\mu\nu} = 0 \quad (2)$$

Here, ∇_μ represents the covariant derivative, u^μ is the four-velocity and $T^{\mu\nu}$ is the stress-energy tensor. $T^{\mu\nu} = \rho h u^\mu u^\nu + P g^{\mu\nu}$ for ideal fluid with h as the specific enthalpy given by $h = 1 + \frac{\Gamma}{\Gamma-1} \frac{P}{\rho}$, $\Gamma = 4/3$ being the adiabatic index. Following {3+1} formalism [23, 24], we write the space-time metric $g_{\mu\nu}$ in terms of lapse (α), shift vector (β^i) and the spatial metric (γ_{ij}). After some algebraic manipulations, this set of equations can be written as a set of five partial differential equations (PDEs):

$$\frac{1}{\sqrt{-g}} \left[\frac{\partial \sqrt{\gamma} D}{\partial t} + \frac{\partial}{\partial x^i} \left(\sqrt{-g} D \left(v^i - \frac{\beta^i}{\alpha} \right) \right) \right] = 0 \quad (3)$$

$$\frac{1}{\sqrt{-g}} \left[\frac{\partial \sqrt{\gamma} S_j}{\partial t} + \frac{\partial}{\partial x^i} \left(\sqrt{-g} \left(S_j \left(v^i - \frac{\beta^i}{\alpha} \right) + P \delta_j^i \right) \right) \right] = T^{\mu\nu} \left(\frac{\partial g_{\nu j}}{\partial x^\mu} - \Gamma_{\nu\mu}^\lambda g_{\lambda j} \right) \quad (4)$$

$$\frac{1}{\sqrt{-g}} \left[\frac{\partial \sqrt{\gamma} \tau}{\partial t} + \frac{\partial}{\partial x^i} \left(\sqrt{-g} \left(\tau \left(v^i - \frac{\beta^i}{\alpha} \right) + P v^i \right) \right) \right] = \alpha \left(T^{\mu 0} \frac{\partial \ln \alpha}{\partial x^\mu} - T^{\mu\nu} \Gamma_{\mu\nu}^0 \right) \quad (5)$$

Here, $\sqrt{-g} \equiv \det(g_{\mu\nu})$ and $\sqrt{\gamma} \equiv \det(\gamma_{ij})$, and these are connected by $\sqrt{-g} = \alpha \sqrt{\gamma}$. We denote the set of five-component vector $U = (D, S_j, \tau)$ as vector of conserved variables and can be expressed in terms of vector of primitive variables $V = (\rho, v^i, P)$ as follows:

$$D = \rho W, \quad S_j = \rho h W^2 v_j, \quad \tau = \rho h W^2 - P - D.$$

Here, W is the Lorentz factor given by $W = 1/\sqrt{1 - v^i v_i} = \alpha u^t$. v^i are the components of three-velocity given as $v^i = \frac{u^i}{\alpha u^t} + \frac{\beta^i}{\alpha}$ and the co-variant counter part can be calculated as $v_j = \gamma_{ij} v^i$.

The above set of PDEs is further written in integral form and subsequently discretised on a given mesh [23, 24]. For our present calculations, we use Schwarzschild space-time metric for which $\alpha = \sqrt{1 - 2/r}$, $\beta^i = 0$, $\sqrt{-g} = r^2 \sin \theta$ and

$\sqrt{\gamma} = r^2 \sin \theta (1 - 2/r)^{-1/2}$. The resulting discretised equations on a spherical mesh constructed using Boyer–Lindquist coordinates (t, r, θ, ϕ) [25] are solved using finite volume method. A better choice may be to use horizon penetrating Kerr-Schild coordinate representation of Schwarzschild metric, which we may adopt in future works.

For spatial reconstruction, we have used second order accurate van Leer slope limiter following [26]. We perform reconstruction on vector (ρ, Wv^i, P) , instead of primitive variable vector V , since the reconstruction on Wv^i ensures sub-luminal reconstructed profile of v^i inside a zone [27]. We have provisions for HLL and LLF Riemann solvers for calculating the interfacial fluxes. Second-order accurate strong stability preserving Runge-Kutta(RK) time integration is used for time advancement. One of the non-trivial step in general relativistic hydrodynamics is conserved-to-primitive conversion as it requires a non-linear equation solution employing a root solver (e.g., Newton-Raphson). We have implemented two methods following [28] and [29]. For our calculations, we prefer the method of [29]. It may happen that the root solver does not converge for a few zones after the time-update step and for such pathetic zones, we use the previous time-step solution as it is already saved in a RK type time-update. The timestep dt is calculated following standard Courant-Friedrichs-Lewy (CFL) condition ([30, 31])

$$dt = C_{\text{CFL}} \frac{1}{\frac{\lambda^r}{dr} + \frac{\lambda^\theta}{r d\theta} + \frac{\lambda^\phi}{r \sin \theta d\phi}},$$

where, λ^i is maximum speed in i^{th} direction and C_{CFL} is the CFL number. For all the runs, we use $C_{\text{CFL}} = 0.9$. For one- or two-dimensional simulations, contribution from the corresponding inactive dimension(s) is switched off.

4 Results

In this section, we present results of a few standard test problems validating our implementation. Later in this section, we present results for couple of production runs for sub-Keplerian accretion disk.

4.1 One-dimensional test problems

In this sub-section, we present results of a couple of test problems to demonstrate the achievement of global accuracy and correctness of our code.

Table 1 Second order convergence for static torus problem

Zones	L_1 error	Accuracy	L_{inf} error	Accuracy
64	5.11×10^{-5}		7.14×10^{-3}	
128	1.58×10^{-5}	1.69	1.99×10^{-3}	1.84
256	3.72×10^{-6}	2.09	1.66×10^{-3}	0.26
512	5.05×10^{-7}	2.88	2.79×10^{-4}	2.57
1024	1.06×10^{-7}	2.26	1.71×10^{-5}	4.03
2048	2.80×10^{-8}	1.92	2.84×10^{-6}	2.56
4096	7.36×10^{-9}	1.93	7.46×10^{-7}	1.93

4.1.1 Stationary torus

In this benchmarking test problem, we initialize a one-dimensional (radial direction) computation domain [4:40] using a constant specific angular momentum ($l = 3.9$), stationary torus solution [32, 33, 34] and evolve the solution for one-full rotation period $t = 100$ at the density maximum. Next, we subtract the numerical solution from the stationary solution and compute the errors. For a globally (i.e., spatially and temporally) second order accurate code, the error should converge with second order accuracy. For this test problem, we run simulations with zones ranging from 64 to 4096. The results are shown in Table 1. Both the L_1 and L_{inf} accuracy columns show achievement of second order accuracy in the asymptotic limit.

4.1.2 Standing accretion and wind shock solutions

In these one-dimensional benchmarking test problems, we demonstrate our code's capability to capture discontinuous solutions that are predicted in [35, 36]. For the black hole accretion (wind) solution having multiple sonic points, it is possible that the solution branch passing through the outer (inner) sonic point is connected to the solution branch passing through the inner (outer) sonic point via a shock transition. Analytically, one needs to perform the Rankine-Hugoniot analysis to find the shock location. Using numerical simulation, we are able to detect the shock at the analytically predicted location with a satisfactory level of accuracy.

Figure 1(a) shows an example of the shock in accretion solution. The solid line shows the analytical solution and the crosses show the numerical solution. The numerical solution is shown at a time $t = 20000$. This simulation is run a one-dimensional radial domain [2.2:100] using 300 ratioed grid (with common ratio = 1.018). We use inflow type boundary condition at the outer radial boundary $r = 100$ and outflow type boundary condition at the inner radial boundary $r = 2.2$. This solution is specified by the specific energy ($\epsilon = 1.007$) and specific angular momentum ($l = 3.4$). The outer sonic point, shock and the inner sonic points are located at 89.6, 27 and 5.4, respectively. The numerical solution clearly captured all this locations. We notice from Figure 1(a) that flow is highly supersonic when it

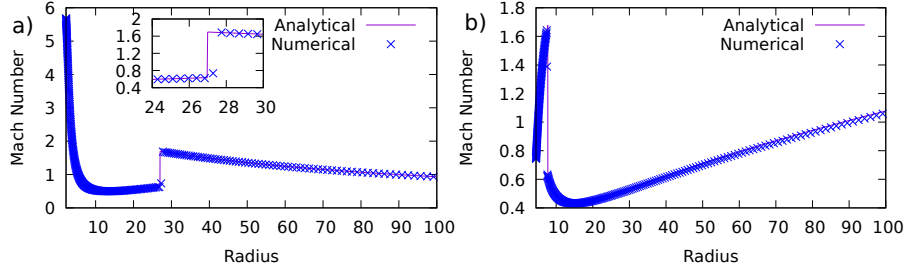


Fig. 1 a) shows the comparison between the analytical (solid line) and the numerical solutions (crosses) for the shock in accretion solution whereas b) shows the same for shock in wind solution. Both the plots show a very good matching between the analytical and numerical results.

crosses the inner boundary. Therefore, acoustic waves do not propagate any feedback upstream from the inner boundary.

Figure 1(b) shows an example of shock in wind solution. The line-point styles are same as in Figure 1(a). Here, the numerical solution is shown at a time $t = 30000$. This simulation is run a one-dimensional radial domain $[4.5:100]$ using 300 ratioed grid (with common ratio = 1.018). We use inflow type boundary condition at the inner radial boundary $r = 4.5$ and outflow type boundary condition at the outer radial boundary $r = 100$. This solution is specified by $\epsilon = 1.007$ and $l = 3.48$. The inner sonic point, shock and the outer sonic points are located at 5.04, 7.7 and 88.23, respectively. Here again, the numerical solution captured all the locations.

4.2 Two-dimensional test problems

In this sub-section, we present results of a couple of test problems to demonstrate the operability of our code in multi-dimensions.

4.2.1 Stationary torus

This is a multi-dimensional extension of the test problem presented in 4.1.1. We initialize a constant specific angular momentum $l = 3.9$ stationary torus on the $r - \theta$ domain $[4:40] \times [0 : \pi]$ using 128 logarithmically binned radial grids and 180 uniform angular grids. The initial condition is evolved till $t = 500 \text{ GM}/c^3$ using outflow boundary conditions on radial boundaries and reflective boundary conditions on polar boundaries. Since the torus solution is a result of hydrostatic equilibrium, it is expected that the torus structure will be well-maintained except the numerical dissipation errors. Figure 2 (a) and (b) show the contours of constant rest mass densities on log scale at the initial and the final times, respectively. The inner-most contour corresponds to $\log_{10}(\text{density}) = -1.25$ and successive contours correspond to -1.5, -2, -3, -4 and -7. The contours maintain their overall structure unchanged except

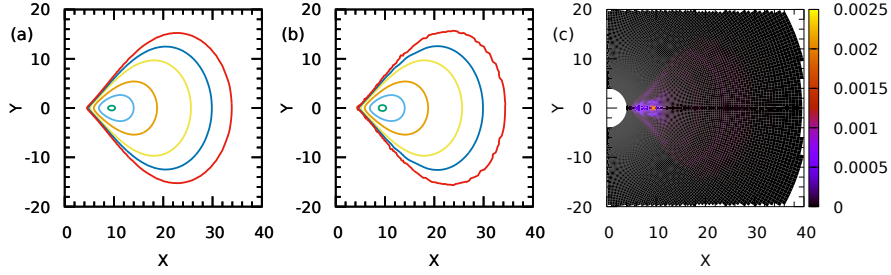


Fig. 2 a) and b) show the contours of constant rest mass densities on log scale at the initial and the final times, respectively. The torus structure is found to be well maintained except towards the outer layers of the torus. c) shows the plot of grid-by-grid difference between the density values. We see difference is highest around the location of density maximum.

a few wiggles on the outer most contour. This is due to the numerical dissipation of our second-order accurate code. Figure 2 (c) shows the grid-by-grid difference of the rest mass density values and we notice that the maximum difference arises at the center of the torus, which is the location of density maximum.

4.2.2 Bondi accretion

In this test problem, we simulate the spherically symmetric Bondi accretion [37] onto a black hole. The simulation is performed on the $r - \theta$ domain $[2.2:100] \times [0 : \pi]$ using 150 logarithmically binned radial grids and 180 uniform angular grids. The simulation domain is initially filled with a background matter having density 10^{-8} times lower than the incoming matter density. We used inflow boundary condition at the outer radial boundary and outflow boundary condition at the inner radial boundary. Thus, at all the ghost zones of the outer radial boundary, we maintain the vector of primitive variables $V = (1.0, -0.05233, 0, 0, 0.005967)$ corresponding to $\epsilon = 1.015$ during the entire simulation.

The simulation is run till the time of $t = 10000$. By this time, a steady state solution is achieved. Figure 3(a) shows the contours of constant Mach numbers whereas (b) shows the rest mass density distribution on log scale at the final time. Both these figures demonstrate the spherical symmetry of the final solution. Figure 3(c) shows the comparison of radial Mach number variation between the analytical (solid line) and the numerical (crosses) results. We find slight mismatch very close to the inner boundary. Here, the gradients of fluid variables are very steep and we believe, to capture the correct solution, we need to use either high order accurate reconstruction schemes or finer resolution if we continue to use second order accurate schemes.

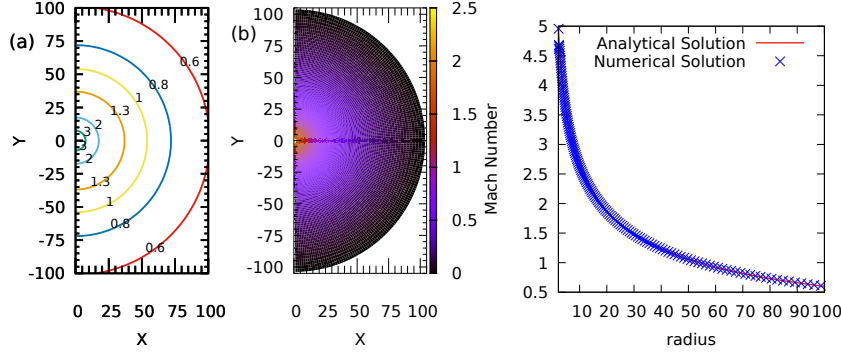


Fig. 3 a) shows the contours of constant Mach numbers whereas b) shows the rest mass densities on log scale at the final time. Both these figures demonstrate the spherical symmetry of the solution. c) shows the comparison of radial Mach number variation between the analytical (solid line) and the numerical (crosses) results.

4.3 Sub-Keplerian accretion disk

In this sub-section, we present results for couple of multi-dimensional simulations of sub-Keplerian accretion disk. We run two cases with two different l values : for run R1, $l = 3.5$ and run R2, $l = 3.56$. $\epsilon = 1.002$ for both the runs. Analytically, these parameters allow shock formation in the sub-Keplerian accretion flow. Because of the higher l value for R2, the average shock location is expected to be at higher radial distance.

For both the cases, the simulations are performed on a $r-\theta$ domain $[2.1:200] \times [0 : \pi]$ using 300 logarithmically binned radial grids and 180 uniform angular grids. The simulation domain is initially filled with a static matter having density and pressure as corresponding floor values (10^{-8} and 10^{-11} respectively). Matter enters the simulation domain at a constant rate through the outer radial boundary. Velocity components and sound speed of the incoming matter are calculated following the analytical solution provided in Section 2 for a given (ϵ, l) pair. Since we don't have radiative cooling or viscous dissipations, incoming matter density ρ_{out} is normalized to 1.0. The sound speed and ρ_{out} together allow one to calculate the pressure of the incoming matter for a given Γ which is $4/3$ for these runs. Thus, the vector of primitive variables V for the incoming matter is calculated using (ϵ, l) pair and this V is maintained at the ghost zones of the outer radial boundary throughout the simulation to mimic constant matter supply to the black hole. This inflow boundary condition is maintained for zones having $80^\circ \leq \theta \leq 110^\circ$. Other than this, we use outflow boundary condition at all other outer radial grids to allow outflow from the accretion disk. We also use outflow boundary condition at the inner radial boundary to mimic free-flow of matter towards the horizon. Simulations are run till a stopping time of $t = 18000$.

Figure 4 shows the time-evolution for run R1. Colors show the density distribution at times a) 400, b) 1600, c) 6000 and d) 18000. Time evolution for run R2 follows

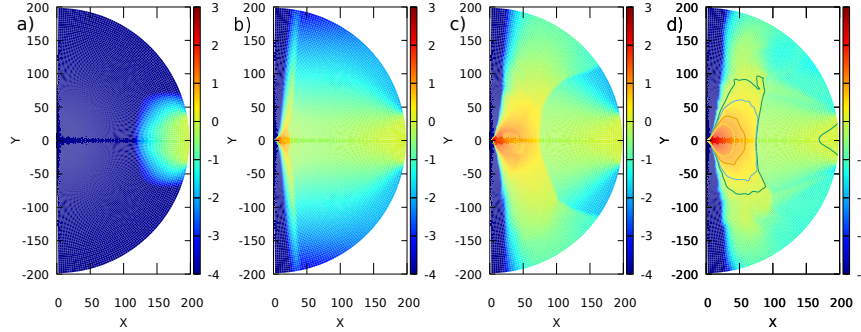
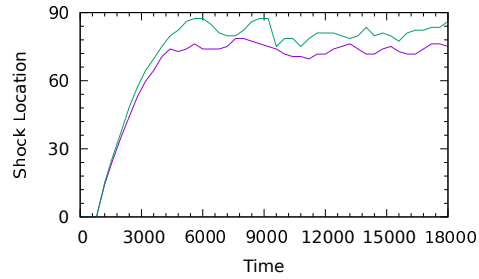


Fig. 4 shows the time evolution of the sub-Keplerian accretion disk structure. Colors show the rest mass density distribution. Snapshots are shown at times a) 400, b) 1600, c) 6000 and d) 18000. Density isocontours corresponding to density values 10, 5, 2 and 1 as we move from inner-most contour to the outer one, are over-plotted in d). The isocontours clearly show the formation of density torus in the post-shock region.

Fig. 5 shows the time variation of the shock location on the equatorial plane for the two different runs (green - R2, purple - R1). This plot shows that the post-shock torus is dynamic rather than being static.



similar pattern. The simulations achieve a nearly steady state around time $t = 6000$ (i.e., state corresponding to Fig. 4(c)). Rest mass density isocontours corresponding to density values 10, 5, 2 and 1 as we move from inner-most contour to the outer one, are over-plotted in Fig. 4(d). The isocontours clearly show the formation of density torus in the post-shock region. The density torus resembles the thick torus which are constructed using hydrostatic equilibrium assumption (e.g., Figure 2). However, our simulated torus has advection included and is highly dynamic. The former is a result of balance between the inward gravitational force and outward combined effect of centrifugal and pressure gradient forces. The flow is purely azimuthal with radial component of four velocity set to zero. However, in our case, the flow has both azimuthal and radial non-zero velocity components. Because of this radial component, energy-momentum is advected towards the black hole. The outer boundary of the torus coincides with the location of shock in the accreting sub-Keplerian matter. Figure 5 shows the time variation of the shock location on the equatorial plane for the two different runs (green - R2, purple - R1). This plot shows that the post-shock torus is dynamic rather than being static. Also, the torus size is larger for higher l . Such post-shock dynamical tori are used to explain the observed spectral and temporal properties of accreting black holes [38, 39, 40, 41].

5 Summary and Conclusions

In this paper, we present our progress of developing a general relativistic fluid dynamics solver. Our aim is to use the said solver for simulating an accretion disk configuration that mimics mass inflow from far out rather than starting from an equilibrium torus. We have demonstrated that our presently developed GRHD code works for Schwarzschild spacetime, is globally second order accurate and performs robustly in multi-dimensions. Finally, using this code, we simulate geometrically thick sub-Keplerian accretion disks. At the time of writing this paper, we have extended the code's operability in three-dimensions and the performance is being tested. We'll report the results in future publications.

Acknowledgements We acknowledge the usage of Kepler cluster of DPS, IISER Kolkata and Pegasus cluster of IUCAA, Pune for running a few simulations. SKG also acknowledges the support of start-up research grant provided by IISER Kolkata. The authors thank the anonymous referee for constructive suggestions for improving the manuscript.

Competing Interests The authors have no conflicts of interest to declare that are relevant to the content of this chapter.

References

1. T.M. Belloni, S.E. Motta, in *Astrophysics of Black Holes: From Fundamental Aspects to Latest Developments, Astrophysics and Space Science Library*, vol. 440, ed. by C. Bambi (2016), *Astrophysics and Space Science Library*, vol. 440, p. 61. DOI 10.1007/978-3-662-52859-4-2
2. H. Netzer, *ARA&A* **53**, 365 (2015). DOI 10.1146/annurev-astro-082214-122302
3. O. Porth, K. Chatterjee, R. Narayan, C.F. Gammie, Y. Mizuno, P. Anninos, J.G. Baker, M. Bugli, C.k. Chan, J. Davelaar, et al., *ApJS* **243**(2), 26 (2019). DOI 10.3847/1538-4365/ab29fd
4. D. Proga, M.C. Begelman, *ApJ* **592**(2), 767 (2003). DOI 10.1086/375773
5. A. Janiuk, D. Proga, R. Kurosawa, *ApJ* **681**(1), 58 (2008). DOI 10.1086/588375
6. J. Li, J. Ostriker, R. Sunyaev, *ApJ* **767**(2), 105 (2013). DOI 10.1088/0004-637X/767/2/105
7. S.M. Ressler, E. Quataert, C.J. White, O. Blaes, *MNRAS* **504**(4), 6076 (2021). DOI 10.1093/mnras/stab311
8. A. Lalakos, O. Gottlieb, N. Kaaz, K. Chatterjee, M. Liska, I.M. Christie, A. Tchekhovskoy, I. Zhuravleva, E. Nokhrina, *ApJ* **936**(1), L5 (2022). DOI 10.3847/2041-8213/ac7bed
9. N. Kaaz, A. Murguia-Berthier, K. Chatterjee, M.T.P. Liska, A. Tchekhovskoy, *ApJ* **950**(1), 31 (2023). DOI 10.3847/1538-4357/acc7a1
10. H. Cho, B.S. Prather, R. Narayan, P. Natarajan, K.Y. Su, A. Ricarte, K. Chatterjee, *ApJ* **959**(2), L22 (2023). DOI 10.3847/2041-8213/ad1048
11. S.K. Chakrabarti, D. Molteni, *ApJ* **417**, 671 (1993). DOI 10.1086/173345
12. D. Molteni, D. Ryu, S.K. Chakrabarti, *ApJ* **470**, 460 (1996). DOI 10.1086/177877
13. D. Ryu, S.K. Chakrabarti, D. Molteni, *ApJ* **474**(1), 378 (1997). DOI 10.1086/303461
14. K. Giri, S.K. Chakrabarti, *MNRAS* **430**, 2836 (2013). DOI 10.1093/mnras/stt087
15. K. Giri, S.K. Garain, S.K. Chakrabarti, *MNRAS* **448**, 3221 (2015). DOI 10.1093/mnras/stv223
16. S.K. Garain, J. Kim, *MNRAS* **519**(3), 4550 (2023). DOI 10.1093/mnras/stac3736
17. B. Paczyński, P.J. Wiita, *A&A* **88**, 23 (1980)
18. J. Kim, S.K. Garain, D.S. Balsara, S.K. Chakrabarti, *MNRAS* **472**(1), 542 (2017). DOI 10.1093/mnras/stx1986

19. J. Kim, S.K. Garain, S.K. Chakrabarti, D.S. Balsara, MNRAS **482**(3), 3636 (2019). DOI 10.1093/mnras/sty2953
20. S.K. Chakrabarti, *Theory of Transonic Astrophysical Flows* (World Scientific Publishing Co, 1990). DOI 10.1142/1091
21. S.K. Chakrabarti, MNRAS **283**, 325 (1996). DOI 10.1093/mnras/283.1.325
22. S.K. Chakrabarti, ApJ **471**, 237 (1996). DOI 10.1086/177965
23. F. Banyuls, J.A. Font, J.M. Ibáñez, J.M. Martí, J.A. Miralles, ApJ **476**, 221 (1997). DOI 10.1086/303604
24. J.A. Font, Living Reviews in Relativity **11**(1), 7 (2008). DOI 10.12942/lrr-2008-7
25. R.H. Boyer, R.W. Lindquist, Journal of Mathematical Physics **8**, 265 (1967). DOI 10.1063/1.1705193
26. A. Mignone, Journal of Computational Physics **270**, 784 (2014). DOI 10.1016/j.jcp.2014.04.001
27. D.S. Balsara, J. Kim, Journal of Computational Physics **312**, 357 (2016). DOI 10.1016/j.jcp.2016.02.001
28. A. Mignone, G. Bodo, MNRAS **364**(1), 126 (2005). DOI 10.1111/j.1365-2966.2005.09546.x
29. L. Del Zanna, N. Bucciantini, A&A **390**, 1177 (2002). DOI 10.1051/0004-6361:20020776
30. R. LeVeque, *Finite Volume Methods for Hyperbolic Problems*. Cambridge Texts in Applied Mathematics (Cambridge University Press, 2002). URL <https://books.google.co.in/books?id=QazcnD7GUoUC>
31. E. Toro, *Riemann Solvers and Numerical Methods for Fluid Dynamics: A Practical Introduction* (Springer Berlin Heidelberg, 2009). URL <https://books.google.co.in/books?id=SqEjX0um8o0C>
32. M. Abramowicz, M. Jaroszynski, M. Sikora, A&A **63**, 221 (1978)
33. S.K. Chakrabarti, ApJ **288**, 1 (1985). DOI 10.1086/162755
34. J.A. Font, F. Daigne, MNRAS **334**(2), 383 (2002). DOI 10.1046/j.1365-8711.2002.05515.x
35. J. Fukue, PASJ **39**(2), 309 (1987)
36. S.K. Chakrabarti, ApJ **337**, L89 (1989). DOI 10.1086/185385
37. H. Bondi, MNRAS **112**, 195 (1952). DOI 10.1093/mnras/112.2.195
38. W. Cui, S.N. Zhang, W. Focke, J.H. Swank, ApJ **484**(1), 383 (1997). DOI 10.1086/304341
39. S.K. Chakrabarti, S.G. Manickam, ApJ **531**(1), L41 (2000). DOI 10.1086/312512
40. D. Radhika, A. Nandi, V.K. Agrawal, S. Mandal, MNRAS **462**(2), 1834 (2016). DOI 10.1093/mnras/stw1755
41. J.R. Shang, D. Debnath, D. Chatterjee, A. Jana, S.K. Chakrabarti, H.K. Chang, Y.X. Yap, C.L. Chiu, ApJ **875**(1), 4 (2019). DOI 10.3847/1538-4357/ab0c1e